Statistical Analysis of GNSS Multipath Errors in Urban Canyons

Matt Peretic
Comms, SIGINT, and PNT Department
The MITRE Corporation
McLean, Virginia, United States
mperetic@mitre.org

Russell Gilabert
Safety Critical Avionics Systems Branch
NASA Langley Research Center
Hampton, Virginia, United States
russell.gilabert@nasa.gov

Dr. Johnson Carroll
Comms, SIGINT, and PNT Department
The MITRE Corporation
McLean, Virginia, United States
jcarroll@mitre.org

Dr. Julian Gutierrez
Safety Critical Avionics Systems Branch
NASA Langley Research Center
Hampton, Virginia, United States
julian.gutierrez@nasa.gov

Dr. Andrew Moore
Dynamic Systems and Control Branch
NASA Langley Research Center
Hampton, Virginia, United States
andrew.j.moore@nasa.gov

Jonathan Christie
Software Eng. and Computing Department
The MITRE Corporation
McLean, Virginia, United States
jchristie@mitre.org

Dr. Evan T. Dill
Safety Critical Avionics Systems Branch
NASA Langley Research Center
Hampton, Virginia, United States
evan.t.dill@nasa.gov

***Abstract*—Much of the prior work studying multipath interference and Non-Line of Sight (NLOS) reception literature studies precise pseudorange error estimation and/or improving a navigation filter's performance in urban canyon environments. This paper instead studies statistical behaviors of pseudorange errors caused by multipath interference and NLOS reception. The error statistics are observed through histograms of known-NLOS measurements collected by a vehicle-mounted commercial Global Navigation Satellite System (GNSS) receiver traveling through a city center. The histograms formed from known-Line of Sight (LOS) measurements generally maintain a zero-mean bias and Gaussian shape, while the histograms from known-NLOS measurements exhibit both greater bias and heavier tails as the canyon depth increases. The histograms show that the NLOS measurements also suffer greater errors in canyons with similar depth on both sides as compared to canyons where the depth of one side is significantly greater. As modern state estimators often incorporate statistical error models to fuse measurements, these specific results offer insights into how to select statistical error models that better match the Radio Frequency (RF) environment which urban GNSS receivers experience.**

***Index Terms*—GPS, GNSS, multipath, NLOS, urban canyon, pseudorange, NavQ, UAS, unmanned aerial system, urban air mobility, UAM, advanced air mobility, AAM**

I. Introduction

Urban canyons prove to be challenging environments for Global Navigation Satellite System (GNSS) receivers due to a variety of factors not present in open-sky environments. Often times, buildings block the Line of Sight (LOS) to satellites, reducing their general availability to the receiver, or worse, the receiver measures and uses Non-Line of Sight (NLOS) reflections of the GNSS signals. Even if the LOS to an individual satellite is not blocked, one or more reflected copies of the GNSS signal can interfere with the LOS signal and distort a receiver's cross-correlation result (known as multipath interference [6]). Multipath interference and NLOS reception can lead to pseudorange errors on the order of tens or even hundreds of meters, which can propagate through the navigation solver and cause reported positions with errors on the order of the urban canyon width, as will be discussed further in Section II.

The manner in which pseudorange errors from multipath interference and NLOS reception vary is of particular concern, as the variations violate key assumptions central to many modern GNSS receiver state estimation techniques. A Kalman filter, which receivers often employ in measurement fusion and navigation-domain filtering, assumes that errors in the system are zero-mean Gaussian. Researchers have proposed many enhancements to the fundamental Kalman filter design to accommodate different error models, and some of these may be good solutions for the types of pseudorange errors in urban canyons, but the pseudorange error behavior must be well-understood to inform navigation risk assessment and the design of receivers capable of meeting integrity requirements for urban missions [13].

This work studies the statistical behavior of empirical urban pseudorange errors. As pseudorange errors vary based on the GNSS signal reflectors and the GNSS signal blockers

This technical data was produced in part for the U. S. Government under Purchase Order 80NSSC24PB490, and is subject to the Rights in Data-General Clause 52.227-14, Alt. IV (DEC 2007). Approved for Public Release; Distribution Unlimited. Public Release Case Number 25-0085.

present at a given location, understanding how the pseudorange error statistics behave for a receiver in the vicinity of those urban features will offer insights to improving urban receiver performance. This study will classify the measurements and study how they vary along the three following dimensions:

1) Whether the measurement is LOS or NLOS
2) The urban canyon depth near the receiver, as quantified by a proposed local urban canyon depth classifier
3) Whether the local urban canyon has similar depth on both sides of the receiver, or whether one side of the canyon is notably deeper, also quantified by the proposed local urban canyon depth classifier

Using these classification dimensions, Section V presents histograms of pseudorange errors individually for different classifications and analyzes trends in their bias and distribution shape. The pseudorange errors are real-world measurements from a commercially-available GNSS receiver in Columbus, Ohio, USA, as described in Section IV. A technique for isolating the pseudorange error caused by multipath interference and NLOS reception from the raw observables which the commercial receiver collects is detailed in Section III. Section II provides the technical background for the multipath interference and NLOS reception error isolation technique and summarizes prior work studying empirically-collected urban pseudorange error analysis.

II. Background

Multipath signals can be primarily characterized by their additional propagation delays. For "near" echoes (when the relative propagation delay with LOS is comparable to the receiver tap spacing), the LOS and near echo also interfere in a manner which distorts the correlation processing and gives rise to signal fading effects [2, Chapter 22]. Characterizing these effects of near echoes interfering with LOS form the basis of most standard approaches to multipath error analysis (see [2, Chapter 22] for an overview of both standard analysis approaches and the associated caveats), and typically lead to a statistical error measure based on the standard deviation of the range error [1], as one component of the User Equivalent Range Error (UERE). However, in a complex urban environment where satellites drop in and out of LOS, the receiver may acquire and track multipath signals with large relative propagation delay. Furthermore, in an urban canyon, this can occur to many satnav signals concurrently, making it difficult to apply traditional mitigation techniques (such as Receiver Autonomous Integrity Monitoring, for example) to reject the affected measurements. This can lead to much larger position errors which are biased along the affected pseudoranges.

Understanding and characterizing these measurement errors is essential for safe usage of GNSS in urban navigation [13]. Many navigation algorithms are based on variations of Kalman filters, which both expect measurement errors to have zero-mean Gaussian distributions and perform poorly when the assumed error distribution parameters do not match the true error distributions. In some cases, non-Gaussian measurement errors can be handled by overbounding with conservative Gaussian distributions, but the distribution parameters must be appropriately chosen based on the true measurement error distribution.

One approach to better characterizing the urban multipath is to directly model the path length of multipath signals using ray tracing at each point in time for the trajectory of interest, but this generally requires more information than is known as is too computationally expensive for most applications. Accurate reflected ray modeling requires detailed information on both the geometry of the reflective surfaces as well as the material characteristics of those surfaces. Performing this modeling along even simple trajectories through an urban environment requires substantial computational resources [11].

A 2018 survey of urban GNSS positioning integrity [13] notes the importance of statistical models when performing navigation risk assessment for urban navigation missions, and the survey discusses several proposed analytical models of urban pseudorange error statistics, but it does not cite any empirically-derived statistical models in the literature. Since then, two recent studies have conducted such analysis. In [4, 12], researchers used a stationary custom receiver architecture to isolate multipath from GNSS signals collected in Shanghai, China, then characterized the distribution of multipath delays relative to the LOS signal. However, NLOS measurements were excluded, and the custom receiver architecture makes it difficult to infer how a typical receiver's measurements would be impacted. More recently, the study presented in [8] collected GNSS data in Toulouse, France, used image processing to classify satellites as LOS and NLOS, then used the distribution of receiver measurements for the LOS and NLOS signals to design receiver-based classification rules. Both works present distributions with non-zero mean bias and heavy tails, but they have limited generalizability, as all of the data are aggregated across their respective collection trajectories without generalization to features of the urban canyon.

Unlike previous approaches, this study analyzes the variation of multipath pseudorange measurement errors with respect to urban canyon features. Characterizing the measurement error distribution with respect to the urban environment itself enables quantitative comparison of different geographic regions and can facilitate design and evaluation of navigation algorithms.

III. Multipath Interference and NLOS Reception Error Isolation Methodology

In order to isolate the pseudorange error from multipath interference and NLOS reception on empirical pseudorange measurements from a GNSS receiver, the test receiver's measurements must first be corrected to remove other sources of error including satellite position error, satellite clock error, receiver clock error, and atmospheric delay [2]. Since this study focuses on the error statistics, this correction methodology can be done in post-processing to aid the isolation accuracy. This analysis leverages the receiver's truth trajectory dataset, final satellite ephemeris information, satellite visibility information

inside the canyons as a function of time and location, and observables from nearby reference receivers.

For this study, the pseudorange measurement logged by the test receiver $\rho^{(k)}(n)$ from satellite with ID k at the receiver epoch n is modeled as:

$$\begin{aligned}\rho^{(k)}(n) = &||\mathbf{x}^{(k)}_{sat,actual}(n) - \mathbf{x}_{rx,actual}(n)|| \\ &+ c(\delta t^{(k)}_{sat,actual}(n) + \delta t_{rx,actual}(n)) \\ &+ \epsilon_{atmospheric}(n) + \epsilon_{relativistic}(n) \\ &+ \epsilon_{rx,noise}(n) + \epsilon_{multipath/NLOS}(n)\end{aligned} \tag{1}$$

where $\mathbf{x}^{(k)}_{sat,actual}$ is the true position of the satellite with ID (k), $\mathbf{x}_{rx,actual}$ is the true position of the receiver, c is the speed of light, $\delta t^{(k)}_{sat,actual}$ is the true clock bias for satellite ID (k), $\delta t_{rx,actual}$ is the true clock bias of the test receiver, $\epsilon_{atmospheric}$ is the error contribution of atmospheric effects including ionospheric and tropospheric, $\epsilon_{relativistic}$ is the error contribution of relativistic effects, and $\epsilon_{rx,noise}(n)$ is the error contribution of thermal noise and unmodelable receiver effects.

The term of interest in this study, $\epsilon_{multipath/NLOS}$, which is the error contribution of multipath and NLOS effects, can be isolated in three steps: removing the satellite-to-receiver geometric range component of the measurement, a common-mode error correction, and a clock error correction.

A. Removing the Geometric Range Component

The receiver truth trajectory dataset provides $\mathbf{x}^{(k)}_{rx,est}$, an estimate of $\mathbf{x}_{rx,actual}$. The satellite broadcast ephemeris provides both $\mathbf{x}^{(k)}_{sat,est}$ and $\delta t^{(k)}_{sat,est}$, estimates of $\mathbf{x}^{(k)}_{sat,actual}$, and $\delta t^{(k)}_{sat,actual}$. Subtracting $||\mathbf{x}^{(k)}_{sat,est} - \mathbf{x}^{(k)}_{rx,est}||$ and $c\delta t^{(k)}_{sat,est}$ from (1) yields a composition of measurement error terms $\epsilon^{(k)}_{meas,1}(n)$, which is the result of the first step of the isolation methodology:

$$\begin{aligned}\epsilon^{(k)}_{meas,1}(n) = &\epsilon^{(k)}_{rx/sat,range}(n) \\ &+ c(\delta t^{(k)}_{sat,actual}(n) + \delta t_{rx,actual}(n)) \\ &+ \epsilon_{atmospheric}(n) + \epsilon_{relativistic}(n) + \epsilon_{rx,noise}(n) \\ &+ \epsilon_{multipath/NLOS}(n)\end{aligned} \tag{2}$$

where $\epsilon^{(k)}_{rx/sat,range}(n)$ is the error in range correction term (as computed by the difference between satellite k's position from the broadcast ephemeris and the receiver truth trajectory) and the range between satellite k's actual position and the receiver's actual position.

B. Common-Mode Error Correction

To correct the control segment and signal propagation modeling errors in (2), the next step employs pseudorange measurement single-differencing. According to the theoretical performance expectations given in [7], for receivers within tens of kilometers of each other and with tens of seconds of signal latency, the biased error terms $\delta t^{(k)}_{sat,actual}(n)$, $\epsilon_{atmospheric}(n)$, and $\epsilon_{relativistic}(n)$ are reduced to tens of centimeters in magnitude and with a zero-mean Gaussian error distribution. Additionally, single differencing cancels out satellite position prediction error. So, after applying single differencing, the term $\epsilon^{(k)}_{rx/sat,range}(n)$ changes to $\epsilon^{(k)}_{truth}(n)$, which is the error in the position reported by the truth trajectory along the straight line distance to satellite k.

This correction does introduce new error sources. The reference receiver which provides the measurements for single differencing will introduce its own receiver thermal noise error $\epsilon_{ref,noise}(n)$. Further, if the reference receiver does not provide clock correction information, a new clock bias term is introduced: $\delta t_{ref,actual}(n)$. Thus, after applying single differencing, and assuming that the reference receiver's clock bias is unknown, the corrected error measurement for the receiver under study $\epsilon^{(k)}_{meas,2}(n)$ becomes:

$$\begin{aligned}\epsilon^{(k)}_{meas,2}(n) = &\epsilon^{(k)}_{truth}(n) \\ &+ c(\delta t_{ref,actual}(n) + \delta t_{rx,actual}(n)) \\ &+ \epsilon_{rx,noise}(n) + \epsilon_{ref,noise}(n) \\ &+ \epsilon_{multipath/NLOS}(n)\end{aligned} \tag{3}$$

C. Clock Error Correction

Assuming that the reference receiver for the single differencing technique has been chosen according to the requirements in [7], and assuming that the truth dataset's position error is within a few meters, $\epsilon_{multipath/NLOS}(n)$, $c\delta t_{ref,actual}(n)$, and $c\delta t_{rx,actual}(n)$ should constitute the majority of the remaining error. Thus, measurements where $\epsilon_{multipath/NLOS}(n)$ is known to be negligible afford an observation of the clock error terms, $\delta t_{ref,actual}(n)$ and $\delta t_{rx,actual}(n)$.

There are multiple ways to find measurements with known-negligible $\epsilon_{multipath/NLOS}(n)$; this work chooses to use the measurements classified as LOS by the satellite visibility modeling for the clock error estimation under the assumption that they have the least $\epsilon_{multipath/NLOS}(n)$. Since the results of this study primarily focus on $\epsilon_{multipath/NLOS}(n)$ for the NLOS-classified measurements, and only the *relative* occurrence and *relative* error biases with respect to the NLOS-classified measurements are needed from the LOS measurements, this is a useful trade-off.

Thus, the third stage of the multipath interference and NLOS reception error isolation technique averages over $\epsilon^{(k)}_{meas,2}(n)$ using only the LOS measurements to generate a time-series of receiver clock corrections. To reduce the impact of the remaining error terms ($\epsilon^{(k)}_{truth}(n)$, $\epsilon_{rx,noise}(n)$, and $\epsilon_{ref,noise}(n)$) on this clock correction time series, the time series can be low-pass filtered, as the other error terms are expected to vary at a higher rate than the receiver clock [3]. Applying this clock correction back to $\epsilon^{(k)}_{meas,2}(n)$ yields the isolated multipath interference and NLOS reception error term $\epsilon^{(k)}_{meas,final}(n)$:

$$\begin{aligned}\epsilon^{(k)}_{meas,final}(n) = &\epsilon^{(k)}_{truth}(n) + \epsilon_{clk,est}(n) \\ &+ \epsilon_{rx,noise}(n) + \epsilon_{ref,noise}(n) \\ &+ \epsilon_{multipath/NLOS}(n)\end{aligned} \tag{4}$$

where $\epsilon_{clk,est}(n)$ is the error in estimation of the clock bias terms $\delta t_{ref,actual}(n)$ and $\delta t_{rx,actual}(n)$.

IV. Experiment Design

Columbus, Ohio, USA was selected to study the statistical behavior of pseudorange errors as a function of the local features. An automobile-mounted u-Blox F9R GNSS receiver with an Ardusimple L1/L2 simpleANT2B-OEM GNSS antenna mounted on the roof of the vehicle collected GNSS observables along the route pictured in Figure 1. The vehicle drove eight laps around the trajectory shown in Figure 1; four laps from 2-4pm Universal Coordinated Time (UTC) on May 11, 2023, and four laps from 2-4pm UTC on May 31, 2023. For simplicity, only the L1 C/A Global Positioning System (GPS) measurements were used in the analysis of Section V; in total, 21,205 GPS L1 C/A pseudorange measurements were collected over this trajectory.

It is important to note that specifics of the u-Blox F9R's design such as tracking loop tap spacing and any potential multipath mitigation techniques do not appear to be publicly disclosed at the time of this writing. Such receiver design specifics will have a significant impact on the multipath interference and NLOS reception error distribution results presented in Section V. However, these results should be generalizable to other receivers of the same model and with known-similar tracking loop architecture and multipath mitigation techniques.

The receiver truth trajectory dataset was derived from the fused multi-GNSS, multi-band, and inertial-aided solution generated by the F9R receiver during data collection. The receiver's solution used L1 and L2 measurements from the GPS, Galileo, BeiDou, and GLONASS satnav constellations. This solution was clamped to $2\,\mathrm{m}$ Mean Sea Level (MSL) above ground, and the latitude and longitude values were manually inspected to ensure correctness.

The International GNSS Service (IGS) station ID ASCO (Delaware, Ohio, USA) was used as a reference receiver for the single differencing required in the multipath interference and NLOS reception error isolation technique described in Section III. The clock error corrections were low-pass filtered with a 6th-order Butterworth filter with a cut-off frequency of $0.2\,\mathrm{Hz}$ according to [3].

In post-processing, the test receiver's measurements were classified as LOS or NLOS by satellite visibility modeling. The specific satellite visibility modeling software, called NavQ, propagates satellite ephemeris information and, by means of shadow-casting over Digital Elevation Map (DEM) data, assesses which satellites are visible over the vehicle's trajectory [5, 10]. The DEM data used in the following analysis was retrieved from a 2019 3DEP LiDAR survey available through the United States Geological Survey (USGS)'s 3DEP LidarExplorer tool [9].

To observe the impact of the local urban canyon features on the statistical behaviors of pseudorange errors, all collected pseudorange measurements are marked with additional local

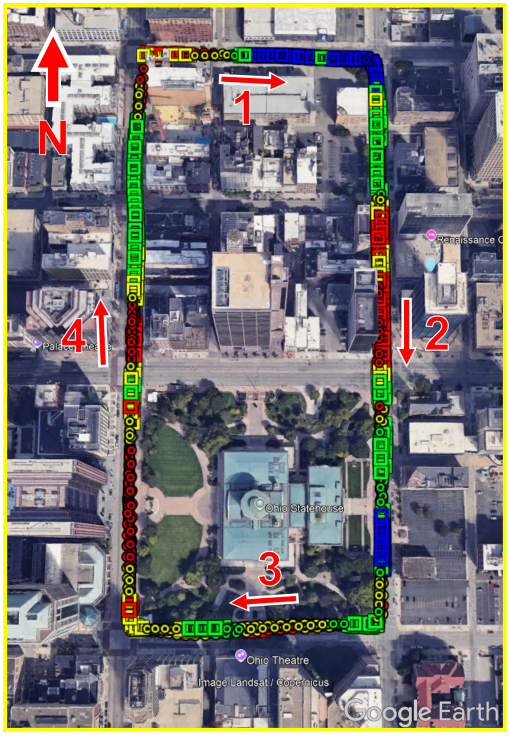

(a) Overhead view of vehicle trajectory.

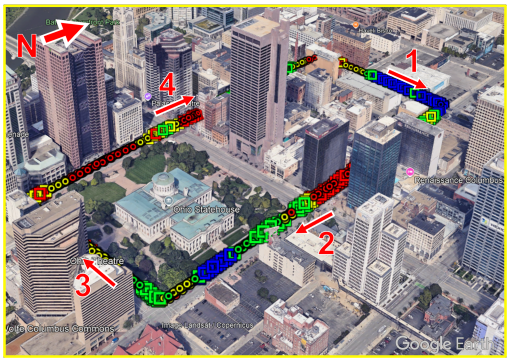

(b) Isometric view of vehicle trajectory.

Fig. 1: Receiver trajectory in the urban data collection. The icon colors indicate canyon depth classification, as given in Table I. Points classified as two-sided canyons are denoted with a square icon, and points classified as a one-sided canyon are denoted with a circle icon. Columbus's street-plus-sidewalk width is consistently roughly $27\,\mathrm{m}$ over the vehicle trajectory.

urban canyon feature descriptors using NavQ. For this, Columbus's urban canyons are modeled as walls on the left and right of the direction of travel of the receiver, and modeled as open terrain ahead and behind the direction of travel of the receiver. For each point in the test receiver's trajectory, the descriptors are derived using the average elevation angles to the top of the canyon walls on the left ($el_{max,L}$) and on the right ($el_{max,R}$) of the direction of travel according to NavQ's urban terrain modeling. Figure 2 shows an example of the canyon classification approach at a given point along the trajectory.

From this, two canyon descriptors are derived for each point in the trajectory. First, the canyon depth is classified according to one of four discrete labels: "Deep", "Moderate", "Shallow", or "Open". The value for receiver epoch n is chosen according to which range in Table I the value $max(el_{max,L}(n), el_{max,R}(n))$ falls within. The specific ranges in Table I were chosen using Kernel Density Estimation (KDE) to cluster all of the $max(el_{max,L}(n), el_{max,R}(n))$ values in the trajectory; the boundaries in Table I closely correspond to the local minima of the KDE results, rounding to the nearest 5° increment. Second, the canyon shape is classified according to one of two discrete labels: "One-sided" or "Two-sided". This is chosen by comparing $|el_{max,L}(n) - el_{max,R}(n)|$ to a threshold of 15°. The canyon is called "Two-sided" if $|el_{max,L}(n) - el_{max,R}(n)|$ is less than 15°, and the canyon is called "One-sided" if not. This closely corresponds to both the center of mass and a local minimum of the KDE results of all of the $|el_{max,L}(n) - el_{max,R}(n)|$ values in the trajectory.

TABLE I: Urban Canyon Classification

Urban Canyon Depth Characterization Label	Max Elevation Angle to Top of Building on Deeper Side of Canyon	Map Icon Color
Open	0 to 30°	Blue
Shallow	30° to 55°	Green
Moderate	55° to 70°	Yellow
Deep	70° to 90°	Red

These discrete classification labels offer a way to identify and group similar regions of the city according to properties of the urban canyon, providing a higher resolution look into the multipath interference and NLOS reception effects on pseudorange errors.

V. Results

The subsequent analysis studies the statistical behavior of the multipath interference and NLOS reception errors in the receiver's pseudorange measurements in the data collected in Section IV.

After applying the multipath interference and NLOS reception error isolation technique as detailed in Section III and classifying all of the measurements as either LOS or NLOS as described in Section IV, various subsets of the measurements are aggregated into histograms. All figures use 2.5 m-wide histogram bins, selected to provide both small enough resolution to observe the shape of the smaller-variance LOS-classified measurement distributions, and large enough resolution to observe the shape of the larger-variance NLOS-classified measurements distributions. Histogram bins are marked with a unique color and hatch pattern according to the transmitting satellite to visualize the per-satellite impact on the overall distribution.

Figure 3 shows the occurrences of the isolated $\epsilon^{(k)}_{meas,final}$ as a function of their value in meters. The top plot of Figure 3, the histogram of $\epsilon^{(k)}_{meas,final}$ values from the LOS-classified measurements, appears Gaussian in shape with a mean near

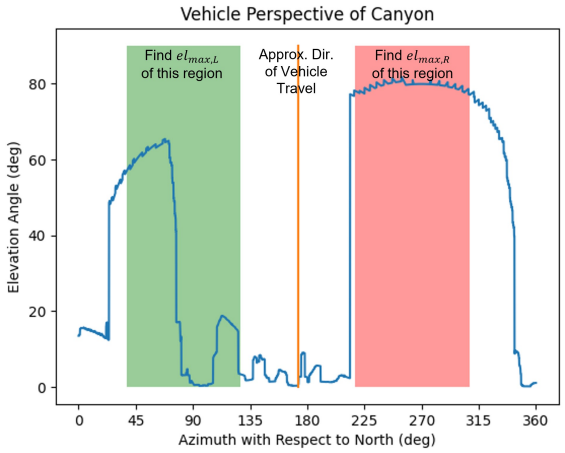

(a) The elevation angle to the top of the canyon walls as a function of azimuth from NavQ. The blue line traces the top-most edge of the visible buildings according to a DEM data model.

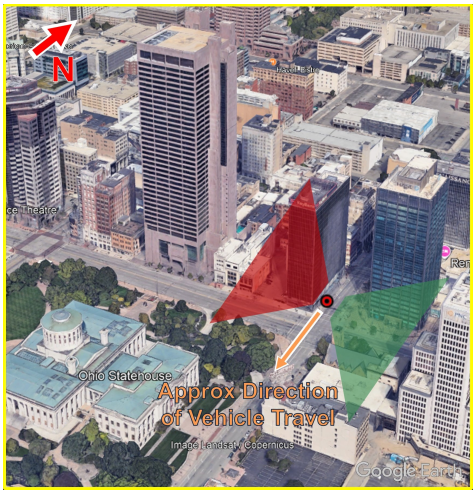

(b) The point in the trajectory assessed in (a) as seen from overhead.

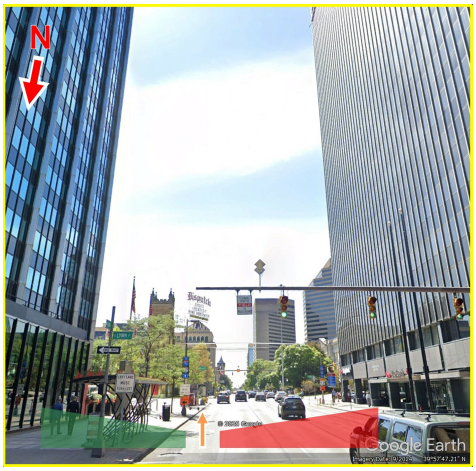

(c) The street view perspective in the trajectory assessed in (a). The point assessed in (a) is roughly 55m forward of the position where this screenshot was taken in order for it to capture the height of the immediately adjacent tall buildings assessed in the green and red regions of (a).

Fig. 2: The canyon walls data used in the measurement classification assessment.

$0\,\mathrm{m}$. In contrast, the $\epsilon^{(k)}_{meas,final}$ values from the NLOS-classified measurements have a long tail in the positive error direction.

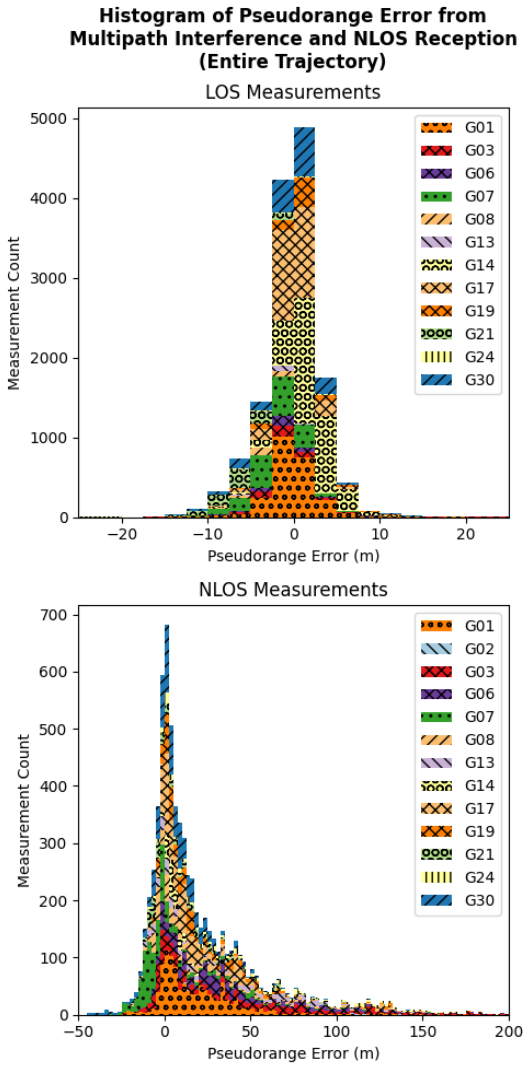

Fig. 3: The $\epsilon^{(k)}_{meas,final}$ value histograms of all LOS-classified (top) and NLOS-classified (bottom) measurements in the dataset. The source satnav signal (designated by Pseudo-random Number (PRN) and a leading "G" character) for a given measurement is assigned a unique color and hatch combination, as indicated in the legend.

For the LOS-classified measurements, this indicates that $\epsilon_{multipath/NLOS}$ is likely Gaussian distributed and/or the majority of the mass of the distribution is likely less than a few meters. Second, the correction terms ($\epsilon_{rx,poserr}(n)$, $\epsilon_{clk,est}(n)$, and $\epsilon_{ref,noise}$) are also likely Gaussian distributed and/or less than a few meters. Thus, since the magnitude of errors in the correction terms should not change whether the measurements are LOS-classified or NLOS-classified, this isolation methodology appears to provide a reasonable observation of $\epsilon_{multipath/NLOS}$ on the order of magnitude of tens of meters.

To analyze the impact of local canyon depth on pseudorange errors caused by multipath interference and NLOS reception, the following plots show histograms of the $\epsilon^{(k)}_{meas,final}$ from the LOS-classified and NLOS-classified measurements classified according to the depth and feature metrics defined in Table I. Figure 4, Figure 5, Figure 6, and Figure 7 show the $\epsilon^{(k)}_{meas,final}$ histograms for all measurements classified as locally "Open", "Shallow", "Moderate", and "Deep" canyon depths, respectively.

As expected, the $\epsilon^{(k)}_{meas,final}$ values from the NLOS measurements exhibit tails in the positive error direction. The majority of the mass of NLOS measurement distributions generally appears between $-25\,\mathrm{m}$ and $100\,\mathrm{m}$. The weight of the tail generally increases with deeper canyon depth classification. Compared to the "Open" and "Shallow" classifications, the "Moderate" and "Deep" classifications show a notable increase in multipath interference and NLOS reception pseudorange errors between $20\,\mathrm{m}$ and $60\,\mathrm{m}$. Some outliers do occur beyond this region. The mass in the tail seems to increase only slightly from the "Moderate" classification to the "Deep" classification. This may indicate that NLOS/multipath error saturates around a certain canyon depth, perhaps because the buildings are so tall relative to the receiver that they block more signals than they reflect. Alternately, this could simply be an artifact of the dataset; for example, the local buildings in the "Deep" classification may be comprised of different materials or be oriented differently with respect to the receiver compared to those in the "Moderate" classification. Further investigation will be required to understand this effect.

There is also a notable mass of $\epsilon^{(k)}_{meas,final}$ values specifically from satellite G03 with roughly $75\,\mathrm{m}$ of error in the "Shallow"-classified NLOS-classified measurements (Figure 5). The large majority of these measurements are from a one-time event in the trajectory when the vehicle was stopped in traffic for a relatively long period of time compared to the vehicle dynamics through the rest of the collection. As the vehicle was stopped, it appears that the tracking loop following G03's signal stayed particularly strongly locked on an NLOS reflection. Measurements from a few other satellites including G06 and G07 experienced this, too, during that event, though their measurement errors varied more, and the measurements from G03 are coincidentally more separated from the others. As expected, this implies that receiver velocity impacts the statistical behavior of pseudorange errors caused by multipath interference and NLOS reception.

Next, Figure 8 and Figure 9 investigate how the canyon shape affects the "Shallow", "Moderate", and "Deep"-classified $\epsilon^{(k)}_{meas,final}$ distributions.

The $\epsilon^{(k)}_{meas,final}$ distributions of the NLOS-classified measurements with a locally "Two-sided" shape show significantly greater mass in the tail compared to those with a locally "One-sided" shape. This could be due to an increased likelihood of reflected signals having even-numbered counts of bounces along the GNSS signal propagation path. GPS signals are right-hand circularly polarized and, in a perfect reflection, the

polarization switches with every bounce. Since GPS antennas are commonly designed to have minimal gain on left-hand circularly polarized signals [2], signal paths with odd numbers of reflections are more likely to appear weak to the receiver, and the receiver is more likely to track signals with an even number of reflections in their propagation path. Assuming all other factors are equal, "Two-sided" canyons should have a greater potential to be a "hall of mirrors" compared to "One-sided" canyons, thus increasing the likelihood of strong GNSS signal reflections, leading to more significant pseudorange errors from the receiver's perspective.

VI. Conclusion

This paper offers insights to the statistical behavior of pseudorange errors caused by multipath interference and NLOS reception as a function of canyon depth. The measurements are classified as either LOS or NLOS using the NavQ ([10]) shadow casting-based satellite visibility modeling software, corrected to remove the major sources of pseudorange error besides the multipath interference and NLOS reception-induced errors and thermal noise-induced errors, and aggregated into histograms.

The resulting histograms show significant shape difference between the LOS and NLOS distributions, indicating that a receiver could employ LOS/NLOS classification from satellite visibility prediction alone to select between different error models. Additionally, in this dataset, two-sided canyons are several times more likely to experience tens of meters of pseudorange error due to multipath interference and NLOS reception compared to one-sided canyons, and greater canyon depth increases the weight of the tails in the NLOS signals. Thus, receiver designers may also find benefit in choosing between different error models depending on these features of the local canyon environment.

One avenue of future work is to pursue the development of multipath interference and NLOS reception error models. Since the NLOS measurements are not well-described as zero-mean Gaussian, fitting the NLOS measurement histograms to various statistical models could inform future research direction. Researchers might consider studying navigation solver design to improve urban performance, such as when and where conventional Kalman filter-based navigation solvers can achieve sufficient performance, what type of statistics to pursue when developing new Kalman filter variants, and when and where other algorithms such as particle filters may be needed instead. Alternately, these statistical models could inform research into urban integrity metrics which either avoid Gaussian assumptions or find tighter Gaussian overbounds for these models.

Another avenue of future work is to advance the generalizability of urban pseudorange error analysis. Since this study parameterizes the results with respect to canyon depth, the authors expect the results from this study to be generalizable to other urban scenarios with buildings constructed from similar materials and to other receivers with tracking loops comparable to the commercial receiver used in this dataset. To generalize further, future work could include parameter sweeps across different tracking loop architectures, vehicle velocity, building materials, and other satnav codes and constellations. Additionally, some cities may have narrower street widths and/or taller canyon height, which would contribute to deeper canyons than captured in this dataset. The discrete levels of the local urban canyon classification could also be further explored, and potentially expanded to include other aspects such as building materials. Lastly, code-minus-carrier techniques might further improve the multipath interference and NLOS reception pseudorange error isolation beyond the techniques employed this study.

Acknowledgment

The authors thank Ryan Cassel (MITRE), Dr. Sharon Marroquin (MITRE), J. Tanner Slagel (NASA), and Sarah Lehman (NASA) for their technical review. The authors also thank Steve Langel (MITRE) for the helpful discussions.

References

[1] *Global Positioning System Standard Positioning Service Performance Standard*. U.S. Dept. of Defense, 5 edition, April 2020. https://www.gps.gov/technical/ps/2020-SPS-performance-standard.pdf.

[2] John W. Betz. *Engineering Satellite-Based Navigation and Timing*. John Wiley & Sons, Ltd, 2015.

[3] Philippe Brocard. *Integrity monitoring for mobile users in urban environment*. PhD thesis, Laboratoire TELECOM. Institut National Polytechnique de Toulouse - INPT, 2016. English. NNT : . tel-01379632.

[4] Xin Chen. Statistical multipath model comparative analysis of different GNSS orbits in static urban canyon environment. *Advances in Space Research*, 62(5):1034–1048, 2018.

[5] Russell Gilabert, Julian Gutierrez, and Evan Dill. Improvements to GNSS positioning in challenging environments by 3DMA lidar informed selective satellites usage. In *Proceedings of the 36th International Technical Meeting of the Satellite Division of The Institute of Navigation (ION GNSS+ 2023)*, pages 2606–2615, Denver, Colorado, September 2023.

[6] Gary A. McGraw, Paul D. Groves, and Benjamin W. Ashman. *Robust Positioning in the Presence of Multipath and NLOS GNSS Signals*, pages 551–589. 2021.

[7] Pratap Misra and Per Enge. *Global Positioning System*. Ganga-Jamuna Press, second edition, 2011.

[8] Eustachio Roberto Matera, Axel Garcia-Pena, Olivier Julien, Carl Milner, and Bertrand Ekambi. Characterization of line-of-sight and non-line-of-sight pseudorange multipath errors in urban environment for GPS and Galileo. In *Proceedings of the 2019 International Technical Meeting of The Institute of Navigation*, pages 177–196, Reston, Virginia, January 2019.

[9] U.S. Geological Survey. USGS Lidar Point Cloud OH_Columbus_2019_B19. https://apps.nationalmap.gov/lidar-explorer/, 2020. Accessed: 2020-02-23.

[10] Evan Dill *et al.* A predictive GNSS performance monitor for autonomous air vehicles in urban environments. In *Proceedings of the 34th International Technical Meeting of the Satellite Division of The Institute of Navigation (ION GNSS+ 2021)*, pages 125–137, St. Louis, Missouri, September 2021.

[11] Julian Gutierrez *et al.* A High-Performance Computing Predictive GNSS Performance Monitor for Autonomous Air Vehicles in Urban Environments. Technical Report 20240009932, NASA Langley Research Center, Hampton, VA, August 2024.

[12] Yuze Wang, Xin Chen, and Peilin Liu. Statistical multipath model based on experimental GNSS data in static urban canyon environment. *Sensors*, 18(4), 2018.

[13] Ni Zhu, Juliette Marais, David Bétaille, and Marion Berbineau. GNSS position integrity in urban environments: A review of literature. *IEEE Transactions on Intelligent Transportation Systems*, 19(9):2766–2779, 2018.

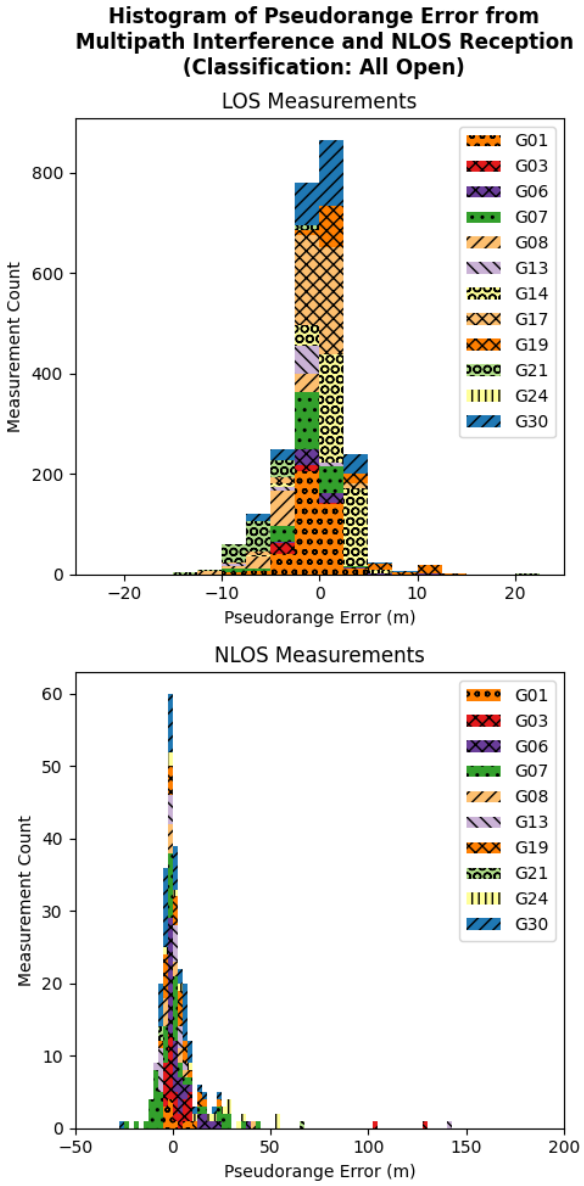

Fig. 4: The $\epsilon^{(k)}_{meas,final}$ value histograms of all LOS-classified (top) and NLOS-classified (bottom) measurements recorded in a locally "Open"-classified canyon.

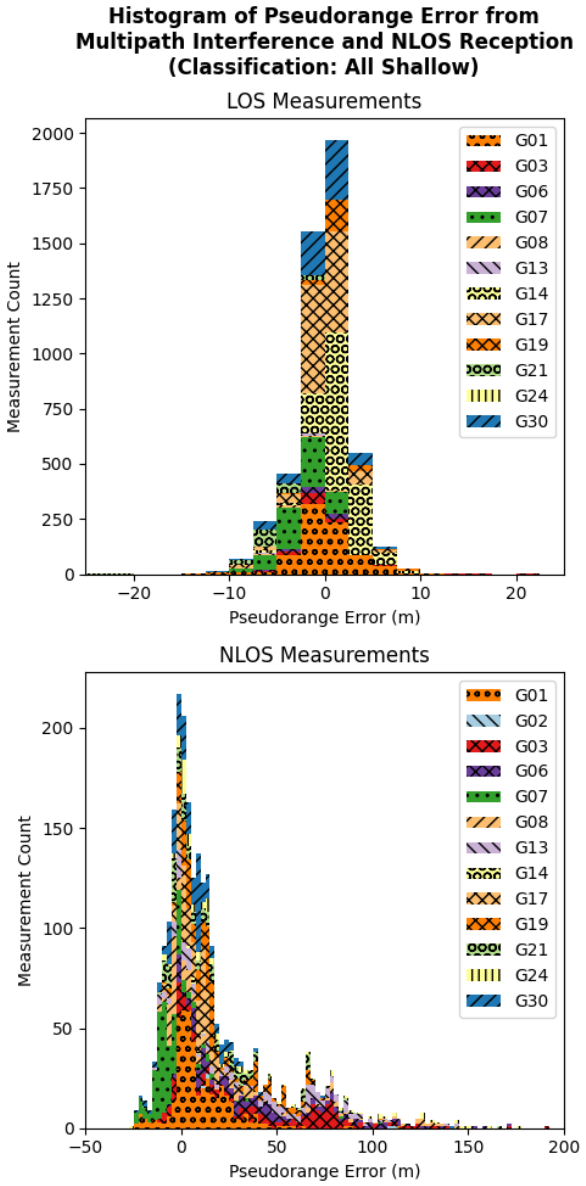

Fig. 5: The $\epsilon^{(k)}_{meas,final}$ value histograms of all LOS-classified (top) and NLOS-classified (bottom) measurements recorded in a locally "Shallow"-classified canyon.

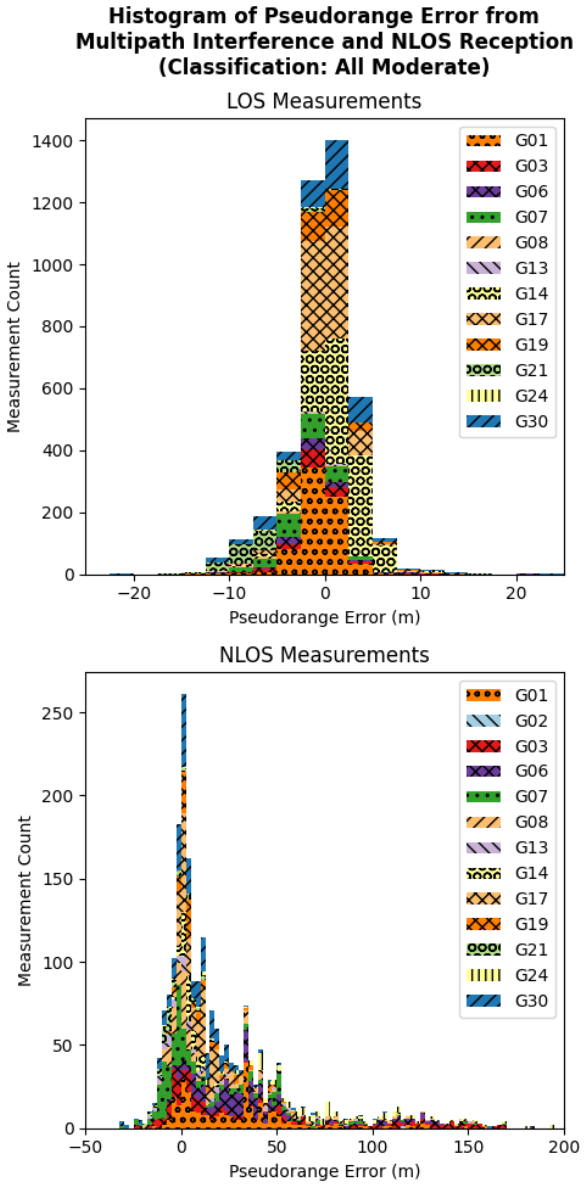

Fig. 6: The $\epsilon^{(k)}_{meas,final}$ value histograms of all LOS-classified (top) and NLOS-classified (bottom) measurements recorded in a locally "Moderate"-classified canyon.

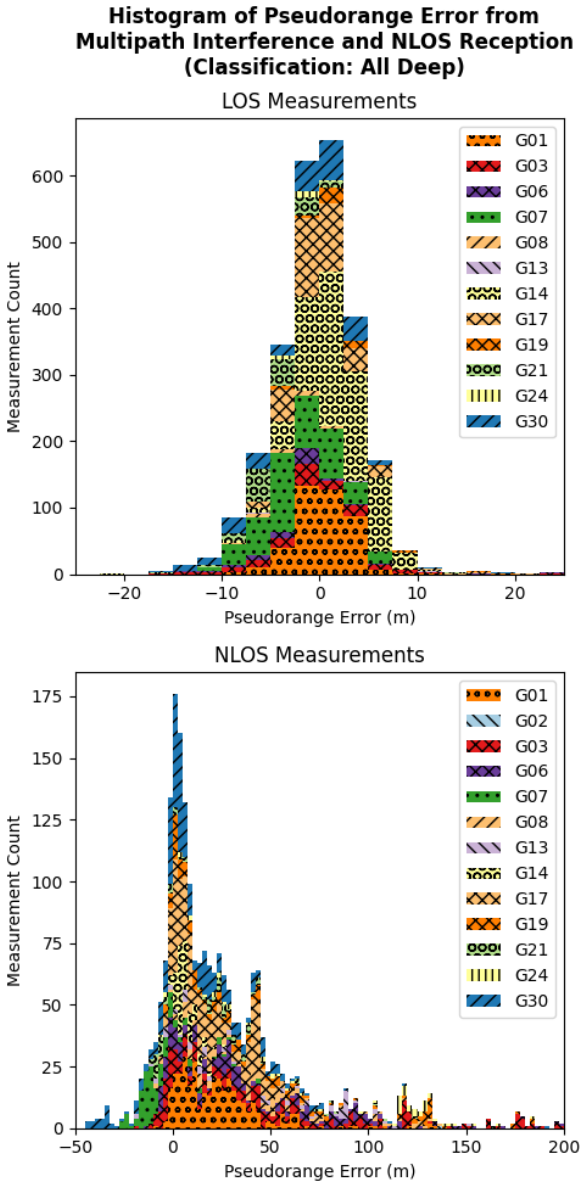

Fig. 7: The $\epsilon^{(k)}_{meas,final}$ value histograms of all LOS-classified (top) and NLOS-classified (bottom) measurements recorded in a locally "Deep"-classified canyon.

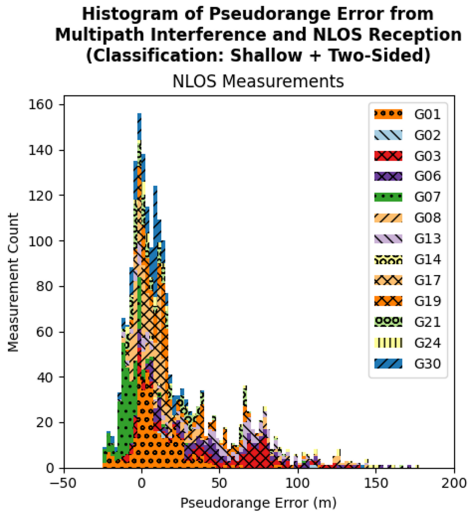

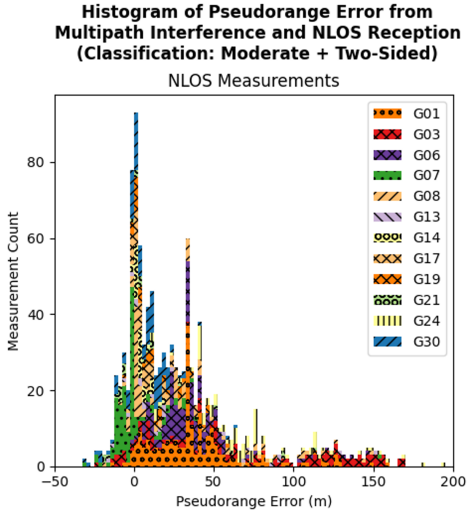

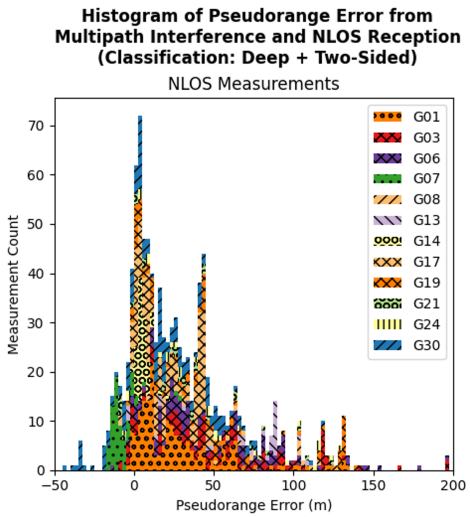

Fig. 8: The $\epsilon^{(k)}_{meas,final}$ values from NLOS-classified measurements at varying canyon depth classifications for two-sided canyons.

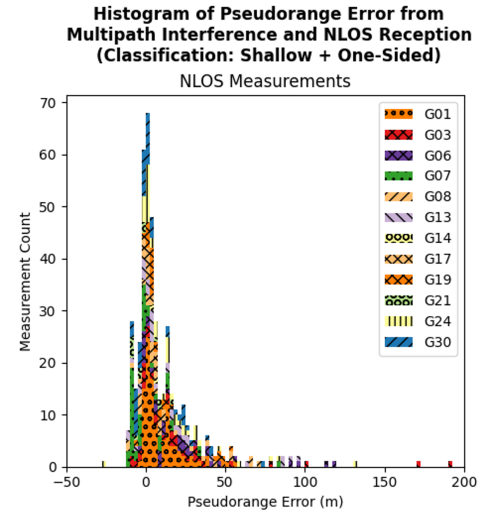

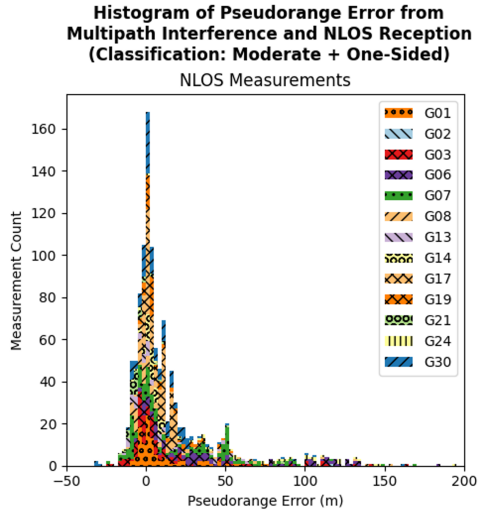

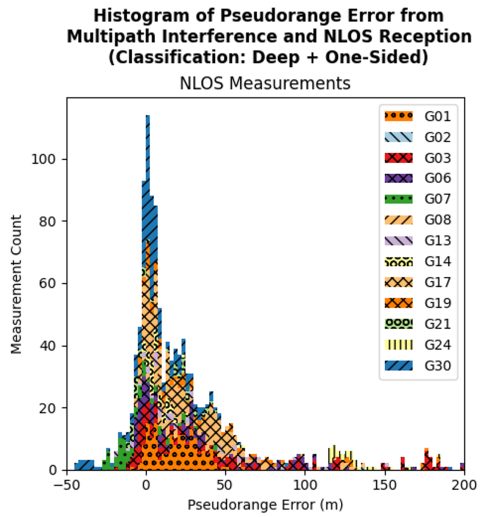

Fig. 9: The $\epsilon^{(k)}_{meas,final}$ values from NLOS-classified measurements at varying canyon depth classifications for one-sided canyons